New insights into the formation of diagenetic illite from TEM studies

Tao Chen,[1, 2]* Hejing Wang,[3] Ting Li,[3] and Nan Zheng[3]

[1]State Key Laboratory of Geological Processes and Mineral Resources, China University of Geosciences, Wuhan 430074, China. *Email:summerjewelry@163.com

[2]Institute of Gemology, China University of Geosciences, Wuhan 430074, China

[3]School of Earth and Space Sciences, Peking University, Beijing 100871, China

Abstract

Diagenetic illite from the Proterozoic Chuanlinggou Formation, China has been investigated using the techniques of transmission electron microscopy (TEM), selected-area electron diffraction (SAED), X-ray diffraction (XRD), scanning electron microscopy (SEM), and energy-dispersive spectrometer (EDS). Polytypes of $1M_d$ and $1M$ illite coexist in the diagenetic illite. The $1M_d$ polymorph is predominant in the <0.2 μm size fraction, which has high Al and low Mg contents and irregular crystal shapes. Lattice-fringe imaging and one-dimensional structural imaging show abundant structure defects. The $1M_d$ illite has both layer and sheet terminations caused by edge dislocations and layer displacements along c^* caused by screw dislocations. These observations indicate that the disordered $1M_d$ structure of the diagenetic illite resulted from abundant dislocations. The dislocation serves as nucleation sites for the illite nano particles to spontaneously nucleate in the initial stage of illite formation. Such a nucleation process obeys the Ostwald ripening rule. The illite only shows a 1.0 nm thickness for each layer

in High-resolution TEM images which suggests that the illite crystals have no mixed smectite layer and the $1M_d$ illites are authigenic and not illitized from smectire or illite/smectite. Heterogeneous nucleation led to directly crystallization of the $1M_d$ illite during the initial growth of illite in shale under a low-temperature and tectonic-stress-free environment. The results have implications for interpreting the distribution of $1M_d$ illite in sedimentary rocks.

KeyWords: diagenetic illite, heterogeneous nucleation, $1M_d$ polymorph, edge dislocation, screw dislocation

Introduction

Nucleation has been widely discussed in material science. It is relevant to the process of crystallization of nanometer sized materials (Abraham 1974; Penn and Banfield 1998; Mendez-Villuendas and Bowles 2007). It is also a subject for scientific investigations in diagenesis, metamorphism, magmatism, and deformation of Earth's materials (Porter and Easterling 2001). Some researchers suggested that nucleation is predominant in the early or initial stage of phyllosilicates' growth (e.g. Baronnet 1992; Baronnet and Kang 1989; Warr and Nieto 1998).

Illite, a phyllosilicate, has a poor crystallinity, deficient interlayer cations, a size of less than 2 μm, and a crystal structure similar to muscovite with a pair of tetrahedral sheets (T sheets) linked by one octahedral sheet (O sheet) in the so-called 2:1 layered structure (Bailey 1984; Rieder et al., 1998). It is widespread in many geological settings of the

Earth's crust, such as diagenesis in mudrocks, very low grade metamorphism and hydrothermal systems, mostly in near-surface and relatively shallow geologic environments, and considered to provide a good record of natural process (Środoń and Eberl 1984; Chen and Wang 2007). A regular sequence of polytypic transition in illite, similar to the dioctahedral mica, from the $1M_d$ through the $1M$ to the $2M_1$ polytype with increasing temperature is well known (e.g., Velde 1965; Grathoff and Moore 1996). Illite has commonly a $1M_d$ structure in its original state of formation (Grubb et al., 1991). There are a lot of evidence suggesting the $1M_d$ illite is a heterogeneous, disordered metastable phase crystallized at low temperature and low pressure conditions (Baronnet 1992; Chen and Wang 2007).

However, whether the $1M_d$ illite originates as a result of direct crystallization or as a replacement of smectite is still controversial. It has been proposed that the authigenic illite formed from the illitization of smectite by a layer-by-layer replacement during burial diagenesis in the Paleozoic pelite or shale with organic matter or fluid played a role in the illitization processes (e.g. Gill and Yemane 1999; Bauluz et al., 2000; Grathoff et al., 2001; Elliott and Haynes 2002). Other mechanisms include formation from a dissolution/crystallization process obeying the Ostwald step rule (e.g. Grubb et al., 1991) and from early 3D-nucleation and 2D-layer growth (e.g. Pandey et al., 1982; Baronnet and Kang 1989).

Lattice imperfection and deformation created during crystal growth or recrystallization can reflect various stages of diagenesis and metamorphism, and a varying

64 physicochemical environment (Ahn and Peacor 1986; Banfield et al., 1994; Jiang et al.,
65 1997). The type and distribution of lattice imperfection are related to specific geological
66 conditions for mineral formation and can help reconstruct the structural mechanism of a
67 phase transformation (Drits 2003; Jiang et al., 1997). Therefore, the lattice imperfection
68 or structure defect of illite is important for studying its formation mechanism.

69 Transmission electron microscopy (TEM) has become the best technique for
70 investigating lattice imperfection in solid-state materials because it is capable of direct
71 observation on microstructure at a nanometer scale in an individual crystal. The
72 occurrence of different polytypes, transformations between polytypes, disordered
73 stacking sequences, lateral-coherent nanodomains, intralayer and interlayer deficiencies,
74 and mixed interlayers in illite have already been successfully studied by TEM, which
75 enriched our knowledge on the crystal structure, growth history and formation
76 mechanism of illite (e.g. Inoue et al., 1988; Grubb et al., 1991; Dong and Peacor 1996;
77 Peacor et al., 2002; Chen and Wang 2007, 2008; Chen et al., 2010).

78 The purpose of this study is to reveal the types of dislocation in diagenetic illite and the
79 mechanism of dislocation formation by direct observation of lattice imperfection and to
80 examine the nucleation process and growth mechanism of the initial formation of the $1M_d$
81 illite in shale.

82

83 **Geologic setting and sample**

84 A suite of Proterozoic strata in the Ming Tombs Section is located on the northeastern

margin of the North China Craton. The stratigraphic sequence of the section with sharp boundaries and simple structures is well preserved, continuously exposed, and unmetamorphosed to slightly metamorphosed. The section is a standard in China, and is one of the several well-preserved sections of the middle Proterozoic strata in the world (Chu et al., 2004; Shi et al., 2008). The Proterozoic strata in this section consist of three groups. The Changcheng Group is the lower one, which displays a typical transition from a near-shore high-energy environment to an off-shore, low-energy setting during the early period of the basin development (Yan and Liu 1998). The Mesoproterozoic Chuanlinggou Formation is characterized by dark to black shales. This formation is well exposed without uplifted at the Jixian County, Tianjin Municipal District, where it contacts conformably with the underlying and the overlying formations (Fig. 1).

The sample used in this study was collected from a layer of yellowish-dark, unweathered silty shale from the Chuanlinggou Formation of the Changcheng Group in the northern part of the Jixian, Tianjin, China (40°11.175' N, 117°29.058' E). The sample consists of illite, chlorite, mixed layer clay minerals [illite/smectite (I/S) and chlorite/smectite (Chl/S)], albite and quartz (Chen and Wang 2007, 2008). The Kübler index of "illite crystallinity" measured on an oriented smear slide is 0.505°Δ2θ indicating that the shale underwent diagenesis rather than metamorphism (Kübler 1968; Frey, 1987; Chen and Wang, 2007).

Analytical methods

106 The sample was crushed into powders and some of the powders were disaggregated in
107 distilled water. Part of the fine powders (<0.2 μm) was air-dried and disaggregated and
108 prepared for XRD analysis of illite polytype by a side-loading method. XRD powder
109 traces were obtained with an X'Pert Pro MPD diffractometer using a Cu Kα radiation at
110 40 kV and 40 mA with an X'cellerator detector (from 4 to 70º 2θ; 0.017º 2θ step size; 20 s
111 per step scanning time).
112 Uncoated fresh fracture surfaces were analyzed directly in a Quanta 200F
113 environmental scanning electron microscope (ESEM) with an accelerating voltage of 15
114 kV. The ESEM is equipped with an energy dispersive spectrometer (EDS) system for
115 determination of the composition of clay minerals.
116 Chemical composition of single illite particle was obtained with an EDAX solid-state
117 EDX detector in an FEI Tecnai F30 scanning transmission electron microscope (STEM),
118 operating at an accelerating voltage of 300 kV. In order to detect the chemical
119 composition of authigenic illite, a small amount of the fine powders (< 0.2 μm) were
120 suspended in alcohol and treated with ultrasound for further dispersal. A drop of the
121 suspension was placed on a copper grid with a carbon film and dried at room temperature.
122 The counting time of EDX analyses was 15 s taking into account composition data
123 reproducibility and electron beam damage. Chemical formulae were calculated based on
124 22 charges and the total structural iron as Fe^{3+}.
125 The portion of the shale sample selected for TEM analysis was prepared as a thin
126 section normal to foliation, first thinned mechanically and finally by argon ion ablation.

TEM was performed at 300 kV using a Hitachi H9000NAR microscope with a point resolution of 0.18 nm (C_s = 0.9 mm). TEM images were recorded on film and the negative was exposed no more than 5 s. HRTEM images were recorded close to the Scherzer defocus from thinned areas near an ion ablation hole and yielded strong contrast images displaying stacking sequences of layers in complex layer structures (Shindo and Hiraga 1998).

Results

XRD analyses of illite polytypes

Sedimentary rocks often contain a mixture of phyllosilicate minerals. Some of the phyllosilicate minerals include more than one polytype. Bailey et al. (1962) first recognized that illite in shale is a mix of detrital mica, its weathering products and diagenetic illite. Later, it is concluded that the detrital mica or illite is of the $2M_1$ polytype, whereas the $1M$ and $1M_d$ are diagenetic (e.g. Velde and Hower 1963; Grathoff et al., 2001; Grathoff and Moore 2002). The $1M_d$ polymorph is predominant in very fine-grained (<1 μm) fractions in the Paleozoic sediments, indicating a low-temperature origin for illite.

We found in this study that polytypes of the $1M_d$ and $1M$ illite coexist in the sample by analyzing the < 0.2 μm randomly oriented tracing (Fig. 2). Whether the randomly oriented tracing can be used to analyze illite polytype is determined by the peak intensity of the 020 and 002 (Grathoff and Moore 1996). In the < 0.2 μm randomly oriented tracing, the peak intensity of the 020 (0.447 nm) is significantly greater than that of the

148 002 (0.500 nm), so the tracing is good enough for analyzing the illite polytype. Moore
149 and Reynolds (1989) considered that the 1*M* and $2M_1$ polytypes of illite have a pair of
150 diagnostic peaks that lie on either side of the illite 003 peak. For the 1*M* polytype, they
151 are the 112 (0.307 nm) and the 11-2 (0.366 nm) {note to typesetting, the minus sign is the
152 bar on top of the 2, hereafter}. For the $2M_1$ polytype, they are the 114 (0.320 nm) and the
153 11-4 (0.349 nm). The "illite hump" [an area of elevated intensity between the 21 and 34º
154 2θ centered on the illite 003 (0.334 nm) position] in the < 0.2 μm randomly oriented
155 XRD trace indicates a small amount of the 1*M* and $2M_1$ polytypes of illite (Moore and
156 Reynolds 1989). However, albite is still in the < 0.2 μm sample, and its main peak
157 overlaps with the 114 peak (0.320 nm) of the $2M_1$ illite (Fig. 2). So the semi-quantitative
158 analysis is only for the 1*M* and $1M_d$ polytypes in this study, and the proportion of the 1*M*
159 polytype to the $1M_d$ one is roughly 1 to 3, that is roughly evaluated from the intensity
160 ratio ($0.26 = I1M/(I1M+I1M_d)$) of the diagnostic reflections of 1*M* (0.307 nm) and $1M_d$
161 (0.259 nm) peaks. Therefore, the $1M_d$ polymorph dominates in the <0.2 μm size fraction
162 of the studied Paleozoic sample.
163

164 **Characteristics of morphology and chemical composition**

165 A loose texture with randomly distributed clay particles shows unevenly foliated grains
166 with irregular grain boundaries (Fig. 3). EDS analyses of the clay particles show
167 abundant Si and Al, with minor amounts of Mg, Fe, K, and Na. Compared with the
168 compositional limits of mica given by the International Mineralogical Association (IMA)

(Rieder et al., 1998), these particles have the chemical composition of illite. Because the smallest electron spot size of the EDS in SEM is too large to analyze a single clay particle, the EDS data are only used to determine the types of clay minerals. The widths of the basal planes of individual illite crystal vary significantly from larger than 2 μm to less than 0.5 μm (Fig. 3).

The EDX analysis in STEM can be treated as contamination-free because it contains only composition information from a scale of dozens of square nanometers. But it cannot determine the amount of H_2O, the valency state of iron or the quantity of Na accurately (Nieto et al., 2010). The chemical compositions of small single particles (< 0.5 μm) yield an average chemical structure formula of $Ca_{0.03}Na_{0.06}K_{0.60}(Al_{1.64}Mg_{0.14}Fe^{3+}_{0.18})_{\Sigma=1.96}(Si_{3.55}Al_{0.45})_{\Sigma=4}O_{10}(OH)_2$ (Table 1). Compared with the structural formula of the 1*M* illite from previous studies, our illite is rich in Al but poor in Mg (Drits et al., 2006; Gualtieri et al., 2008; Peacor et al., 2002).

Lattice imperfections observed by lattice-fringe imaging

Small crystal size and high defect density are characteristics of diagenetic illite (Jiang et al., 1997). TEM with lattice-fringe imaging is one of the best methods to characterize the layer stacking defects of phyllosilicate such as illite. Figure 4a was obtained with the electron beam along the [hk0] incidence, showing the illite crystals comprised of several sub-parallel thin packets within 10 layers stacking and each (00l) lattice fringe is 1.0 nm of spacing. Low-angle boundaries, shown as the layer terminations in the sequences

marked by the white arrows in Figure 4a, are clearly visible between illite crystals. Hiraga et al., (2004) concluded that the interface of low-angle grain boundaries is atomically sharp and very narrow (~1.0 nm) and does not contain amorphous material. This conclusion applies well to the close intergrowth of illite packets. The TEM lattice fringe images have relatively different contrasts among the sub-parallel illite packets, indicating small-scale variations in the orientation of these crystallites.

The inset SAED pattern in Figure 4a shows well-defined 00l reflections with 1.0 nm periodicity corresponding to one layer period polytypism. The diffused non-00l reflections (where k≠3n) streaking parallel to c^* reflect a largely-disordered stacking sequence. It indicates that the crystal has a typical $1M_d$ illite structure (Grubb et al., 1991; Jiang et al., 1997). However, there are several additional weak non-00l diffusing reflections among the 00l reflections and the brightest diffused non-00l reflections resulted from the sub-parallel illite packets with various orientations.

Figure 4b is a diagram illustrating the arrangement of edge dislocations in illite that results in layer termination. The dark lines represent the illite layers stacking along c^*. The dislocation lines of edge dislocations lie within the *ab* plane (parallel to the [hk0] direction) and their Burgers vectors are normal to the *ab* plane (parallel to c^*).

An illite crystal with high-defect density and no more than 40 layers obtained along the [hk0] incidence is shown in Figure 5. The lattice fringes of the illite have a typical mottled texture of varying image contrasts over a short distance (dozens of nanometers), implying variable orientations among nanodomains (Iijima and Buseck 1978). The

211 continuity of illite layers is interrupted within dozens of nanometers by various
212 displacements along *c**, forming wavy layer fringes.

213 The SAED pattern (at the right side of Fig. 5) with well-defined 00l reflections shows a
214 1.0 nm periodicity. These (00l) reflections extend perpendicular to *c** and appear as short
215 arcs (indicated by white arrows) indicating some structure defects existing along *c**,
216 which matches with the layer displacements shown in the lattice fringe image.

217

218 **Structure defects observed by one-dimensional structural imaging**

219 Buseck and Iijim (1974) reported for the first time the one-dimensional HRTEM
220 structure imaging of a mica layer with three dark lines corresponding to two tetrahedral
221 (T) sheets and one octahedral (O) sheet and the brightest line corresponding to the
222 interlayer (I) region. Although it is not used as often as the conventional TEM lattice
223 fringe imaging and the HRTEM near-atomic imaging (also called two-dimensional
224 structural imaging) in mica or illite microstructure studies, one-dimensional HRTEM
225 structure imaging is a better method to provide details of the structural defects of layers,
226 especially the stacking faults of sheets (Shindo and Hiraga 1998). One-dimensional
227 HRTEM images can be obtained with all [hk0] directions, while the near-atomic images
228 require special incident directions such as [100], [110]/[1-10] and their equivalent
229 incidences (Chen and Wang 2007).

230 Figure 6 shows a one-dimensional structure image of a diagenetic illite with three
231 straight, parallel and well-defined dark lines representing a unit illite layer with a 1.0 nm

thickness. The short dark bars at right side of the image indicate the interlayer region. Three dark lines are discontinuous along the (00l) plane because of the complex interlaced sheets shown as the nano-area surrounded by white oval. The long white solid lines marked in the left interlayer regions and the long white dotted lines marked in the right interlayer regions illustrate the displacements of illite layers along c^*.

Edge dislocation with integral Burgers vector makes the atoms in the crystal to slide along integral multiples of the interplanar distance, as shown by those illite layer terminations in Fig. 4a. However, tetrahedral sheet terminations are also observed (marked by the white arrows in the middle part of Fig. 6), indicating the existence of edge dislocations with non-integral Burgers vectors in the $1M_d$ illite. Dislocation does not end inside the crystal but reach the grain surface (Penn and Banfield 1998). Unfortunately, the beam damage has made the surface area of the illite particle amorphous and the details of the defects are lost (shown by the bottom arrow).

Figure 7a is a one-dimensional structure image showing three lateral-coherent illite nanodomains with complex interlaced sheets. Three dark lines represent a unit layer in the illite nanodomains on both sides of the image. The two regions surrounded by the white ovals show the same structural defects as those in Figure 6. The middle illite nanodomain has four dark lines corresponding to a unit illite layer with a 1.0 nm layer thickness. The high-magnification images of the three-dark-line unit layer and the four-dark-line unit layer are compared in Figure 7b. It is obvious that the additional dark lines (marked by white asterisks) correspond to the interlayer regions. It is already known

253 that the interlayer cations in mica and illite are a line of dark spots in near-atomic
254 imaging (Kogure 2002; Chen and Wang 2007). The interlayer cation sheet showing as a
255 dark line in such a four-dark-line unit layer has never been reported.

256 Schematic interlayer cation sheet of an illite with the upper and lower oxygens are
257 illustrated in Figure 7c to explain the reason that the interlayer cation sheets were
258 observed as dark lines in one-dimensional structure imaging. Interlayer cations of
259 muscovite and illite can only be observed as dark spots in the near-atomic imaging
260 exactly along one of the six indices ([100], [110]/[1-10] and their equivalent incidences)
261 (Kogure 2002; Chen and Wang 2010) because the density of the interlayer cations along
262 these six projected directions is the highest and the volume of the electronic charge
263 potential is high enough to be taken on (Shindo and Hiraga 1998). For the same reason,
264 the interlayer cation sheets could be observed as dark lines along these six incident
265 directions in the one-dimensional structure imaging. Therefore, the illite unit layer can be
266 observed as four dark lines along these incident directions. It is common that the illite
267 unit layer is shown as three dark lines corresponding to the TOT sheets when the
268 electronic beam direction deviates from these six incident directions. Figure 7a suggests
269 the electronic beam is exactly parallel to one of these six incidences for the middle
270 nanodomain and deviates from these incidences for the lateral-coherent nanodomains. It
271 indicates that there are small rotation angles among the three lateral-coherent illite
272 nanodomains by revolving around c^*.

273 White solid lines and dotted lines are marked on some interlayer regions of these three

nanodomains (Fig. 7a) to clarify layer displacements. The amounts of displacements are different for the lateral-coherent nanodomains. This phenomenon is equivalent to what has been observed in Figure 5 and 6. Figure 7d is a diagram illustrating how the displacement of layers formed by the screw dislocations between two attached nanodomains. In this case, the Burgers vectors and the dislocation lines are all parallel to c* ([001]*). It indicates screw dislocations exist not only in the $2M_1$, $3T$ or long-period polytype in mica (e.g., Pandey et al., 1982; Kuwahara et al., 2001), but also in the polytype of $1M_d$ illite.

Discussion

Disordered diagenetic $1M_d$ illite

Systematic identification of mica polytypes was described by Ross et al. (1966) based on the possible layer-stacking sequences with relative layer rotations about an axis (c*) perpendicular to the (001) of 0°, ±60°, ±120°, and ±180°. The disordered $1M_d$ polytype has been considered as the $1M_{r\text{-}n(120)}$ (n=0, 1 or 2) with randomly layer stacking sequences along c* (Pandey et al., 1982; Amouric and Baronnet 1983). Pure diagenetic illites are mainly of the so-called $1M_d$ polytype, which progressively evolves toward the $2M_1$ (Grubb et al., 1991; Nieto etal., 2010). In our early study, we observed the $1M_{r\text{-}n(120)}$ illite structure with the near-atomic imaging (Chen and Wang 2007), such a disordered structure attributes to randomly stacking sequences along c*.

In the present study, the XRD tracing of the <0.2 μm size samples and the SAED

patterns indicates that illite is mainly of the $1M_d$ polytype with a large amount of structural defects. The sample has a lot of small illite crystals with uneven basal planes and irregular grain boundaries as revealed by the SEM images. Chemical composition analyses reveal large amounts of Al substituted for Si in the tetrahedral sites while occupies the octahedral sites. All of these observations suggest abundant defects existing in the diagenetic $1M_d$ illite.

The HRTEM imaging revealed imperfect structures with abundant screw and edge dislocations in the disordered illites. They show similar SAED patterns but different HRTEM images to those of the $1M_{r\text{-}n(120)}$ illite. We conclude that the diagenetic $1M_d$ illite has more complex disordered structures in the Paleozoic shale. The disordered structure was not only caused by randomly stacking sequences along c^* but also resulted from deformation induced dislocations.

Dislocation generation caused by imperfect oriented attachment

Jiang et al. (1997) used the TEM and XRD analyses to show the diagenetic illite is defect-rich, fine-grained (mean thickness by volume=c. 70 nm), $1M_d$ material. In their lattice-fringe images of the $1M_d$ crystals, the illite commonly displays layer terminations, which were interpreted as expressions of edge or screw dislocations. Warr and Nieto (1998) provided a schematic block diagram to illustrate various types of lattice imperfection, including layer termination and dislocation lines, in illite and chlorite observed with the TEM lattice-fringe imaging. Eggleton and Gerald (2011) reported the

316 illite domain separated by layer-terminating defects with an interlayer gap beyond the
317 dislocations. It is similar to what is shown in Figure 4. Moreover, screw dislocations were
318 observed in complex polytypes of mica and considered as the origin of spiral growth.
319 Screw-dislocation theory is powerful in explaining the generation of polytypes (e.g.
320 Amouric and Baronnet 1983; Baronnet and Kang 1989). However, the mechanism of
321 dislocation generation is poorly discussed for illite and mica structures.

322 Penn and Banfield (1998) studied dislocation generation mechanism in a nano-sized
323 scale by using nanocrystalline titania particles coarsened under hydrothermal conditions.
324 They proposed that there will be a driving force to form chemical bonds between the
325 atoms of opposing surfaces to achieve a full coordination when two structurally similar
326 surfaces of particles approach. Because surfaces are not atomically flat, coherence will be
327 achieved by distortions in some places of the interface. Such distortions or dislocations
328 generated from oriented attachment at specific crystallographic surfaces have a small
329 misorientation at the interface (called imperfect oriented attachment). The imperfect
330 oriented attachment of nanocrystals can generate dislocations with edge, screw, and
331 mixed characters. They further suggested edge dislocations are formed when the axis of
332 rotation is contained within the plane of the interface, while screw dislocations will be
333 formed when the axis of rotation is perpendicular to the plane of the interface (Burgers
334 vector parallel to the dislocation line). However, an imperfect attachment involving
335 simple rotation of two particles about an axis normal to the interface has not been directly
336 observed in their study.

Our HRTEM illite study supports the conclusions suggested by Penn and Banfield (1998). Illite consists of stacked layers on the (001) or *ab* planes, which can be considered as the specific crystallographic crystal faces. We have shown the existence of edge and screw dislocations in the diagenetic $1M_d$ illite. There are two ways for the imperfectly oriented nano-packets or nanodomains to attach on illite *ab* plane and to generate different types of dislocations. When coherent illite nano-packets or sheets have rotated slightly about axes parallel to (i.e., within) the *ab* plane, there is a small misorientation along *c** (normal to the *ab* plane) that permits the generation of edge dislocations. The edge dislocations with an integer Burgers vector are shown in Figure 4 and those with a non-integer Burgers vector are shown in the middle part of Figure 6. However, when two attached nanodomains are slightly rotated about *c** (i.e., the axis of rotation is perpendicular to the *ab* plane), there is a small misorientation along the [hk0] that permits the generation of screw dislocations in the illite crystal. They are shown in Figure 5 to 7 by the layer displacements along *c**. Figure 7a is the best HRTEM image showing the small rotation around *c** between the lateral-coherent nanodomains. These two types of imperfect oriented attachments generate abundant edge and screw dislocations with a range of Burgers vectors in the diagenetic illite to form the $1M_d$ polytype.

Nucleation processes in the initial growth of illite

Illite and a sequence of interstratified illite-smectite (I/S) often coexist in the diagenetic

zones. Phase transition from smectite or I/S to illite is well known as the mechanism of illite formation (Inoue et al., 1988; Bauluz et al. 2002; Maraschin et al., 2010). Bauluz et al. (2000) used the TEM imaging to show that the lateral transitions among the I/S sequences are consistent with the illitization by layer-by-layer replacement, and suggested that I/S coexists with illite in the higher-grade diagenetic pelites. We observed order and disorder I/S in our early HRTEM study (Chen and Wang 2008). However, the HRTEM imaging of this study only shows a 1.0 nm thickness for each layer suggesting that the illite crystals have no mixed smectite layer and the $1M_d$ illites do not come from the phase transition of illitization from parent minerals, such as smectite or I/S.

Amouric and Baronnet (1983) found a few nuclei with the 1*M* structure coexisting with disordered ones during the early nucleation of synthetic muscovite polytypism. Baronnet and Kang (1989) considered short-period polytypes (basic structures) and the disordered layer-stacking sequences of mica originate during the early 3D-nucleation and the 2D-layer growth. Indirect evidence has been provided for the growth of the $1M_{r\text{-}n(l20)}$ and 1*M* in phlogopite as well as the 1*M* and $2M_1$ in muscovite during the earlier 3D-nucleation and the subsequent 2D-nucleation processes of the layered modules.

Nucleation exists in the initial step of crystal formation and phase transformation. There are typically two types of nucleation, homogenenous nucleation and heterogeneous nucleation (Porter and Easterling 2001). All nucleation in rocks is effectively heterogeneous. Nucleation needs two important conditions. One is suitable heterogeneous nucleation sites, which can be non-equilibrium defects such as dislocations, grain

boundaries and free surfaces. The other is nanometer-sized material with dimensionally similar surfaces, which allow crystallization in nucleation process (Mendez-Villuendas and Bowles 2007; Penn and Banfield 1998). When adjacent nano-sized particles spontaneously self-organize, they will share a common crystallographic orientation at a planar interface. Such oriented attachment is imperfect oriented attachment, which will have a small misorientation at the interface and generate a range of dislocations (Penn and Banfield 1998).

As illustrated in Figures 5-7 and discussed above, nanodomains of illite are lateral-coherent with screw dislocations. These screw dislocations serve as nucleation sites. Then, the illite nano-particles nucleate side-by-side in three-dimension on their *ab* planes with imperfect oriented attachment and coalesce during growth. If the illite particles are only nano-sized along *c**, these nano-packets will nucleate and coalesce by edge dislocations (as shown in Fig. 4). This bonding between the particles reduces overall energy by removing the surface energy associated with the unsatisfied bonds, and needs complete elimination of the mineral-air or mineral-fluid interface (Penn and Banfield 1998).

Chemical heterogeneity and structure disorder of phyllosilicates, such as illite, imply they do not reflect thermodynamic equilibria under diagenetic conditions (Arkai 2002). Eberl et al. (1990) suggested clay minerals commonly undergo recrystallization by the Ostwald ripening. Essene and Peacor (1995) also suggested that diagenesis reactions are strongly controlled by kinetic factors and obey the Ostwald step rule. The Ostwald step

rule states a system in a state of metastable equilibrium will proceed via steps toward a state which has minimum free energy, whereby the smallest crystallites dissolve and reprecipitate onto larger crystallites in order to minimize the interfacial free energy (Inoue et al., 1988; Altaner and Ylagan 1997). Therefore, the nucleating formed the $1M_d$ illite also can be explained by the Ostwald ripening rule to some extent.

Penn and Banfield (1998) suggested this nucleation mechanism may apply when particles nucleate side-by-side on a substrate and coalesce during growth, but they considered this case is easier for particles that are free to move (such as in solution or where particles have abundant surface-bound water). Eberl et al. (1990) suggested clays may undergo the Ostwald ripening when exposed to fluids such as ground water or hydrothermal solutions, although this process must occur slowly at near-surface temperatures because clays are insoluble. However, according to Środoń and Eberl (1984), solid phase transformation rather than dissolution and crystallization is the ruling mechanism in phyllosilicate evolution. Therefore, fluids may be one of factors in illite nucleation processes.

In conclusion, we suggest heterogeneous nucleation is a way of direct crystallization for the initial growth of the $1M_d$ illite in shale under a low-temperature and tectonic stress-free environment. The results suggest why $1M_d$ illite distributes in sedimentary rocks. However, the influence of fluids acting on its initial nucleation and the possible origin of the fluids as well as the timing of illite formation are needed to be understood with more details to improve the nucleation theory of the initial growth of the $1M_d$ illite.

Acknowledgments

We thank Richard F. Yuretich (Univ of Massachusetts, USA), Necip Guven, and Junfeng Zhang and Roger Mason (China Univ. of Geosciences, China) for constructive comments and suggestions that improved our manuscript. The electron microscopy was carried out in the Electron Microscope Laboratory of School of Physics, Peking University. This research was supported by the National Natural Science Foundation of China (Grant No. 41172050, and 40702007), and by the higher education-research project of Hubei Province (2009108) and the Natural Science Foundation of Hubei Province (2009CDA004).

References

Abraham, F.F. (1974) Homogeneous nucleation theory, 263 p. Academic, New York.

Ahn, J.H. and Peacor, D.R. (1986) Transmission and analytical electron microscopy of the smectite-to-illite transition. Clays and Clay Minerals, 34, 165-179.

Altaner, S.P. and Ylagan, R.F. (1997) Comparison of structural models of mixed-layer illite/smectite and reaction mechanisms of smectite illitization. Clays and Clay Minerals, 45, 517-533.

Amouric, M. and Baronnet, A. (1983) Effects of early nucleation condition on synthetic muscovite polytypism as seen by high-resolution transmission electron microscopy. Physics and chemistry of Minerals, 9, 146-159.

Arkai, P. (2002) Phyllosilicates in very low-grade metamorphism: transformation to

442 micas. In A. Mottana, F.P. Sassi, J.B. Thompson, Jr., and S. Guggenheim, Eds., Micas:
443 Crystal chemistry and metamorphic petrology, 46, p. 463-478. Reviews in Mineralogy
444 and Geochemistry, Mineralogical Society of America, Chantilly, Virginia.
445 Bailey, S.W., Hurley, P.M., Fairbairn, H.W., and Pinson, W.H. (1962) K-Ar dating of
446 sedimentary illite polytypes. Geological Society of America Bulletin, 73, 1167-1170.
447 Bailey, S.W. (1984) Crystal chemistry of the true micas. In S.W. Bailey, Eds., Micas, 13,
448 p. 13-60. Reviews in Mineralogy, Mineralogical Society of Amercia, Washington, D.C.
449 Banfield, J.F., Bailey, S.W., and Barker, W.W. (1994) Polysomatism, polytypism, defect
450 microstructures, and reaction mechanisms in regularly and randomly interstratified
451 serpentine and chlorite. Contributions to Mineralogy and Petrology, 117, 137-150.
452 Baronnet, A. (1992) Polytypism and stacking disorder. In P.R. Buseck, Eds., Minerals and
453 Reactions at the Atomic Scale: Transmission Electron Microscopy, 27, p. 231-238.
454 Reviews in Mineralogy, Mineralogical Society of America, Washington, D.C.
455 Baronnet, A. and Kang, Z.C. (1989) About the origin of mica polytypes. Phase transitions,
456 16, 477-493.
457 Bauluz, B., Peacor, D.R., and Lopez, J.M.G. (2000) Transmission electron microscopy
458 study of illitization in pelites from the Iberian Range, Spain: layer-by-layer replacement?
459 Clays and Clay Minerals, 48, 374-384.
460 Bauluz, B., Peacor, D.R., and Ylagan, R.F. (2002) Transmission electron microscopy
461 study of smectite illitization during hydrothermal alteration of a rhyolitic hyaloclastite
462 from Ponza, Italy. Clays and Clay Minerals, 50(2), 157-173.

463 Buseck, P.R. and Iijim, S. (1974) High resolution electron microscopy of silicates.
464 American Mineralogist, 59, 1-21.
465 Chen, T. and Wang, H.J. (2007) Determination of layer stacking microstructures and
466 intralayer transition of illite polytypes by high-resolution transmission electron
467 microscopy (HRTEM). American Mineralogist, 92, 926-932.
468 Chen, T. and Wang, H.J. (2008) Mix-layer clay minerals from Chuanlinggou Formation
469 of Changcheng System in Jixian County, Tianjin City. Earth Science-Journal of China
470 University of Geosciences, 33(5), 716-722. (in Chinese with English abstract)
471 Chen, T., Wang, H.J., Mason, R., and Chen, L. (2010) HRTEM investigation of intralayer
472 and interlayer stacking defects and pyrophyllite interlayers in illite. Mineralogical
473 Magazine, 74, 451-461.
474 Chu, X.L., Zhang, T.G., Zhang, Q.R., Feng, L.J., and Zhang, F.S. (2004) Carbon isotopic
475 variations of Proterozoic carbonates in Jixian, Tianjin, China. Science in China series
476 D-Earth sciences, 47(2), 160-170.
477 Dong, H. and Peacor, D.R. (1996) TEM observations of coherent stacking relations
478 insmectite, I/S and illite of shales: Evidence for MacEwan crystallites and dominance
479 of $2M_1$ polytypism. Clays and Clay Minerals, 44, 257-275.
480 Drits, V.A. (2003) Structural and chemical heterogeneity of layer silicates and clay
481 minerals. Clay Minerals, 38, 403-432.
482 Drits, V.A., McCarty, D.K., and Zviagina, B.B. (2006) Crystal-chemical Factors
483 responsible for the distribution of octahedral cations over trans- and cis-sites in

484 dioctahedral 2:1 layer silicates. Clay and Clay minerals, 54(2), 131-152.

485 Eberl, D.D., Srodof, J., Kralik, M., Taylor, B.E., and Peterman, Z.E. (1990) Ostwald
486 ripening of clays and metamorphic minerals. Science, 248, 474-477.

487 Eggleton, R.A. and Gerald, J.F. (2011) Illite from muloorina, south australia. Clays and
488 clay minerals, 59(6), 608-616.

489 Elliott, W.C. and Haynes, J.T. (2002) The chemical character of fluids forming diagenetic
490 illite in the Southern Appalachian Basin. American Mineralogist, 87, 1519-527.

491 Essene, E.J. and Peacor, D.R. (1995) Clay mineral thermometry—A critical perspective.
492 Clays and Clay Minerals, 43, 540-553.

493 Frey, M. (1987) Very low-grade metamorphism of clastic sedimentary rocks. Pp. 958 in:
494 Low- Temperature Metamorphism. (Frey, M. editor). Blackie, Glasgow, London.

495 Gill, S. and Yemane, K. (1999) Illitization in a Paleozoic, peat-forming environment as
496 evidence for biogenic potassium accumulation. Earth and Planetary Science Letters,
497 170, 327-334.

498 Grathoff, G.H. and Moore, D. (2002) Characterization of the Waukesha Illite: A
499 mixed-polytype illite in the Clay Mineral Society repository. American Mineralogist,
500 87, 1557-1563.

501 Grathoff, G.H., Moore, D.M., Hay, R.L., and Wemmer, K. (2001) Origin of illite in the
502 lower Paleozoic of the Illinois basin: Evidence for brine migrations. Geological Society
503 of America Bulletin, 113(8), 1092-1104.

504 Grathoff, G.H. and Moore, D.M. (1996) Illite polytype quantification using WILDFIRE©

505 calculated X-ray diffraction patterns. Clays and Clay Minerals, 44, 835-842.
506 Grubb, S.M.B., Peacor, D.R., and Jiang, W. -T. (1991) Transmission electron microscope
507 observations of illite polytypism. Clays and Clay Minerals, 39, 540-550.
508 Gualtieri, A.F., Ferrari, S., Leoni, M., Grathoff, G., Hugo, R., Shatnawi, M., Pagliad, G.,
509 and Billinged, S. (2008) Structural characterization of the clay mineral illite-1*M*.
510 Journal of Applied Crystallography, 41, 402-415.
511 Hiraga, T., Anderson, I.M., and Kohlstedt, D.L. (2004) Grain boundaries as reservoirs of
512 incompatible elements in the Earth's mantle. Nature, 427, 699-703.
513 Iijima, S. and Buseck, P.R. (1978) Experimental study of disordered mica structures by
514 high-resolution electron microscopy. Acta crystallographica, A34, 709-719.
515 Inoue, A., Velde, B., Mennier, A., and Touchard, G. (1988) Mechanism of illite formation
516 during smectite-to-illite conversion in a hydrothermal system. American Mineralogist,
517 73(11-12), 1325-1334.
518 Jiang, W.-T., Peacor, D.R., Árkai, P., Tóth, M., and Kim, J.W., (1997) TEM and XRD
519 determination of crystallite size and lattice strain as a function of illite crystallinity in
520 pelitic rocks. Journal of Metamorphic Geology, 15, 267-281.
521 Maraschin, A.J., Mizusaki, A.Maria., and Zwingmann, H. (2010) Illite authigenesis in
522 sandstones of the Guaritas Allogroup (Early Paleozoic): Implications for the
523 depositional age, stratigraphy and evolution of the Camaqua Basin (Southern Brazil).
524 Journal of South American Earth Sciences, 29, 400-411.
525 Kogure, T. (2002) Investigation of micas using advanced TEM. In A. Mottana, F.P. Sassi,

526 J.B. Thompson, Jr., and S. Guggenheim, Eds., Micas: Crystal chemistry and
527 metamorphic petrology, 46, p. 281-312. Reviews in Mineralogy and Geochemistry,
528 Mineralogical Society of America, Chantilly, Virginia.
529 Kübler, B. (1968) Evaluation quantitative du metamorphisme par la cristallinite de l'iilite.
530 Bulletin du Centre de Recherches de Pau SNPA, 2, 385-397 (in French).
531 Kuwahara, Y., Uehara, S., and Aoki, Y. (2001) Atomic force microscopy study of
532 hydrothermal illite in Izumiyama pottery stone from Arita, Saga Prefecture, Japan.
533 Clays and Clay Minerals, 49(4), 300-309.
534 Mendez-Villuendas, E. and Bowles, R.K. (2007) Surface nucleation in the freezing of
535 gold nanoparticles. Physical Review Letters, 98 (18), 185503-1-185583-4.
536 Moore, D.M. and Reynolds, R.C. (1989) X-ray Diffraction and the Identification and
537 Analysis of Clay Minerals, 332 p. Oxford, New York.
538 Nieto, F., Mellini, M., and Abad, I. (2010) The role of H_3O^+ in the crystal structure of
539 illite. Clays and Clay Minerals, 58, 238-246.
540 Pandey, D., Baronnet, A., and Krishna, P. (1982) Influence of the stacking faults on the
541 spiral growth of polytype structures in mica. Physics and Chemistry of Minerals, 8,
542 268-278.
543 Peacor, D.R., Bauluz, B., Dong, H., Tillick, D., and Yan, Y. (2002) Transmission and
544 analytical electron microscopy evidence for high Mg contents of 1M illite: Absence of
545 1M polytypism in normal prograde diagenetic sequences of pelitic rocks. Clays and
546 Clay Minerals, 50, 757-765.

Peng, Y.B., Wang, D., Yuan, X.L. (2007) Ultrastructure of spheroidal acritarchs from the chuanlinggou formation of the Changcheng system. Acta Micropalaeontologica Sinica, 24(2): 194-204. (in Chinese with English abstract)

Penn, R. L. and Banfield, J. F. (1998) Imperfect oriented attachment dislocation generation in defect-free nanocrystals. Science, 281, 969-971.

Porter, D.A. and Easterling, K.E. (2001) Phase Transformations in Metal and Alloys (Second Edition), 514 p. Chapan & Hall, London.

Rieder, M., Cavazzini, G., D'Yakonov, Y., Frank-Kamenetskii, V.A., Gottardi, G., Guggenheim, S., Koval', P.V., Müller, G. Neiva, A.M.R., Radoslovich, E.W., Robert, J-L., Sassi, F.P., Takeda, H., Weiss, Z., and Wones, D.R. (1998) Nomenclature of the micas. The Canadian Mineralogist, 36, 905-912.

Ross, M., Takeda, H., and Wones, D.R. (1966) Mica polytypes: systematic description and identification. Science, 151, 191–193.

Shi, X.Y., Jiang, G.Q., Zhang, C.H., Liu, J., and Gao, L.Z. (2008) Sand veins and microbially induced sedimentary structures from the black shale of the Mesoproterozoic Chuanlinggou Formation (ca. 1.7 Ga) in North China: implications for methane degassing from microbial mats. Earth Science-Journal of China University of Geosciences, 33(5), 577-590 (in Chinese with English abstract).

Shindo, D. and Hiraga, K. (1998) High-resolution electron microscopy for materials science, 190 p. Springer, New York.

Środoń, J. and Eberl, D.D. (1984) Illite. In: P.H. Ribbe, Eds., Micas, 13, p. 4495-544.

568 Reviews in Mineralogy, Mineralogical Society of America, Washington, D.C.

569 Velde, B. (1965) Experimental determination of muscovite polymorph stabilities.
570 American Mineralogist, 50, 436-449.

571 Velde, B. and Hower, J. (1963) Etrological significance of illite polymorphism in
572 paleozoic sedimintary rocks. American Mineralogist, 48(11-12), 1239-1254.

573 Wang, H., Wang, H.J., Chen, T., and Zhang, Z.Q. (2005) Study of Two-dimensional
574 Nanometer Illite in Jixian County, Tianjin City. Geological Review, 51(3), 319-324. (in
575 Chinese with English abstract)

576 Warr, L. and Nieto, F. (1998) Crystallite thickness and defect density of phyllosilicates in
577 low temperature metamorphic pelites A TEM and XRD study of clay mineral
578 crystallinity index standards. The Canadian Mineralogist, 36, 1453-1474.

579 Yan, Y.Z. and Liu, Z.L. (1998) On the relationship between biocommunities and
580 Paleoenvironments in Changcheng Period of the Yanshan Basin, North China. Acta
581 MicroPaleontologica Sinica 15, 249-266.

582

583 **Figure Captions**

584 **Figure** 1. Geological sketch of Jixian region (modified from Wang et al., 2005; Peng et
585 al., 2007).

586 Q-Quarternary; Є1f-Fujunshan Formation of Lower Cambrian; Qbj-Jingeryu Formation;
587 Qbx-Xiamaling Formation; Jxt-Tieling Formation; Jxh-Hongshuizhuang Formation;
588 Jxw-Wumishan Formation; Jxy-Yangzhuang Formation; Chg-Gaoyuzhuang Formation;

589 Chd-Dahongyu Formation; Cht-Tuanshanzi Formation; Chch-Chuanlinggou Formation;
590 Chc-Changzhoucun Formation; Arq-Qianxi Group of Archean.
591
592 **Figure** 2. Random oriented XRD tracings of <0.2 μm samples. Some reflection peaks of
593 illite are labeled. The main peak of albite (Ab) overlaps with the 114 peak of $2M_1$ illite.
594 Other unlabelled peaks are reflections of illite. Peak at 0.307 nm belongs to 1*M* polytype
595 and peak at 0.259 nm belongs to $1M_d$ respectively.
596
597 **Figure** 3. SEM image of illite showing two distinct sizes of illite crystals with uneven
598 basal (001) plane and irregular outline.
599
600 **Figure** 4. (a) Lattice-fringe image of several subparallel illite packets obtained along
601 [hk0]. Layer termination is marked by white arrow. The SAED pattern contains
602 well-defined 00l reflections and streaking non-00l reflections (where $k \neq 3n$) which
603 indicate a disordered stacking sequence. (b) Diagram illustrates layer termination caused
604 by edge dislocation between sub-parallel illite packets. "**b**" is Burgers vector. *c**
605 corresponding to layer stacking direction. "⊙"corresponding to rotation axes of illite
606 packets, which is normal to paper.
607
608 **Figure** 5. Lattice-fringe image showing mottled structure indicating high density of
609 defects in the $1M_d$ illite. Lateral-coherent nanodomains with different contrast show layer

610 displacement along *c**. A nanodomain is surrounded by a white rectangle and is
611 magnified at the upper left. In the SAED pattern, streaking non-00l reflections are caused
612 by stacking disorder of layers, and short arc-like 00l reflections (marked by white arrows)
613 are caused by defects (e.g., layer displacement) along *c**.
614
615 **Figure** 6. One-dimensional structure image obtained along [hk0] incidence showing T, O,
616 T sheets represented by three dark lines and the interlayer region represented by the
617 brightest line. Short dark bars at the right side mark on interlayer regions, and the white
618 oval surrounds some complex interlaced sheets. Long white solid lines and dotted lines
619 marked on interlayer regions illustrate illite layers displace along *c**. Two white arrows in
620 the middle part indicate sheet termination. The white arrow at the bottom indicates a
621 defect reaching the surface of the illite crystal.
622
623 **Figure 7.** (a) One-dimensional structure image of three lateral-coherent illite
624 nanodomains. The white ovals surround complex interlaced sheets. Both sides of the
625 nanodomains show three dark lines corresponding to T, O, T sheets, while the middle
626 nanodomain shows four dark lines. The additional dark line marked by white asterisks.
627 The white solid and dot lines mark on interlayer regions. (b) Comparison of illite unit
628 layers represented by three dark lines (left) and four dark lines (right) to illustrate the
629 additional dark line corresponds to interlayer sheet. (c) A schematic presentation of
630 interlayer cations (represented by dark gray balls) with upper and lower oxygens

631 (represented by light gray balls) along [001]. (d) Diagrammatic representation of screw
632 dislocation generates from sheet displacement of two imperfectly oriented attached
633 nanodomains. Two nanodomains are represented by small black dots and circles
634 respectively, which do not correspond to exact atom sites. *c** corresponds to layer
635 stacking direction. Dotted arrows refer to the axes of rotation of closely spaced domains.

TABLE 1. Chemical composition of illite in Chuanlingguo Formation obtained by EDX in STEM

Testing spots	1	2	3	4	5	6	s.d.	Ave.
Oxide(%)								
SiO_2	57.54	57.62	62.76	54.44	55.70	56.60	2.87	57.44
Al_2O_3	28.04	28.05	20.89	32.66	31.05	30.95	4.20	28.61
Fe_2O_3	3.08	2.29	8.35	3.36	4.13	2.16	2.30	3.89
MgO	2.74	2.43	0.58	1.00	0.95	1.70	0.87	1.57
K_2O	6.44	8.72	7.31	8.39	8.04	6.75	0.92	7.61
NaO_2	2.02	0.66	n.d.	n.d.	n.d.	0.16	0.96	0.47
CaO	0.12	0.22	0.10	0.15	0.15	1.67	0.62	0.40
Chemical formula								
Si	3.55	3.57	3.89	3.38	3.45	3.48	0.18	3.55
$Al^{[IV]}$	0.45	0.43	0.11	0.62	0.55	0.52	0.18	0.45
$Al^{[VI]}$	1.59	1.62	1.41	1.76	1.72	1.72	0.13	1.64
Fe^{3+}	0.14	0.11	0.39	0.16	0.19	0.10	0.11	0.18
Mg	0.25	0.22	0.05	0.09	0.09	0.16	0.08	0.14
K	0.51	0.69	0.58	0.66	0.63	0.53	0.07	0.60
Na	0.24	0.08	0.00	0.00	0.00	0.02	0.10	0.06
Ca	0.01	0.01	0.01	0.01	0.01	0.11	0.04	0.03
Statistical charge								

Cht	-0.45	-0.43	-0.11	-0.62	-0.55	-0.52	0.18	-0.45
Cho	-0.31	-0.37	-0.48	-0.06	-0.10	-0.25	0.16	-0.27
Chi	0.76	0.80	0.59	0.68	0.65	0.77	0.08	0.72

Notes: s.d. is standard deviation. Ave. is average. n.d. is not detected. Cht is the total charges in tetrahedron. Cho is the total charges in octahedron. Chi is the total cations in interlayer region.

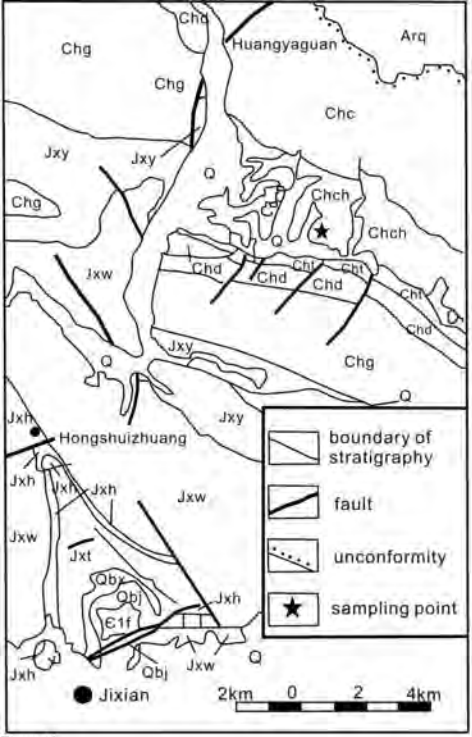
Chg
Huangyaguan
Arq
Chg
Chc
Jxy
Jxy
Chg
Q
Chch
Chch
Jxw
Chd
Chd
Cht
Chd
Cht
Chd
Jxy
Chg
Q
Jxh
Hongshuizhuang
Jxy
Jxh
Jxh
Jxh
Jxw
Jxw
Jxt
Qbx
Qbj
Jxh
∈1f
Jxh
Qbj
Jxw
Q
Jixian
2km 0 2 4km
boundary of stratigraphy
fault
unconformity
sampling point

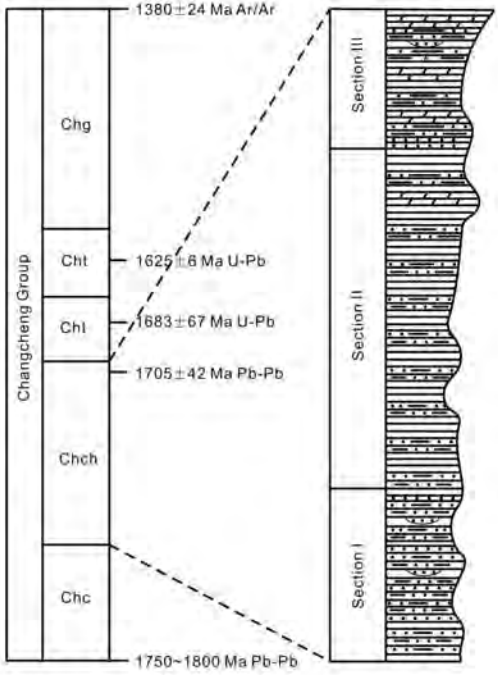
Changcheng Group
Chg
Cht
Chl
Chch
Chc
1380±24 Ma Ar/Ar
1625±6 Ma U-Pb
1683±67 Ma U-Pb
1705±42 Ma Pb-Pb
1750~1800 Ma Pb-Pb
Section III
Section II
Section I
Shale
Silty shale
Pelitic siltstone
Siltstone
Dolomicrite
1 km

Figure1

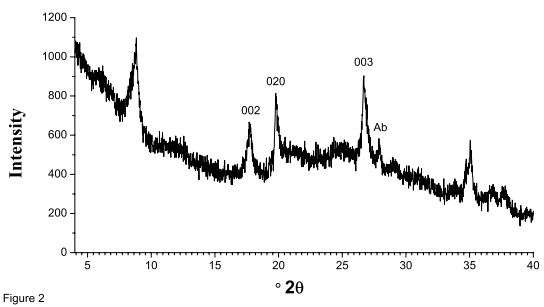
Intensity
1200
1000
800
600
400
200
0
5
10
15
20
25
30
35
40
002
020
003
Ab
° 2θ

Figure 2

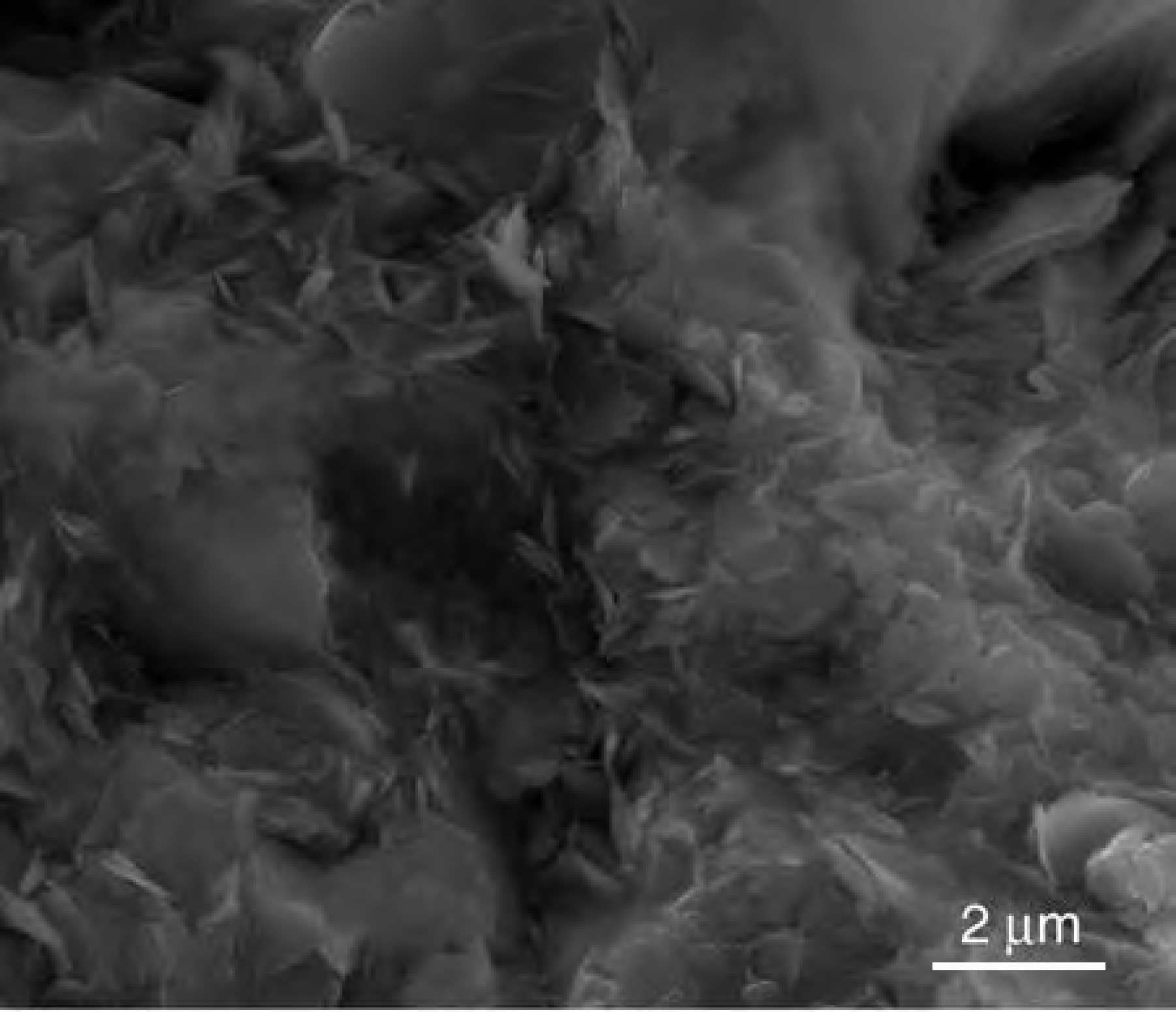

Figure 3

Figure 4a

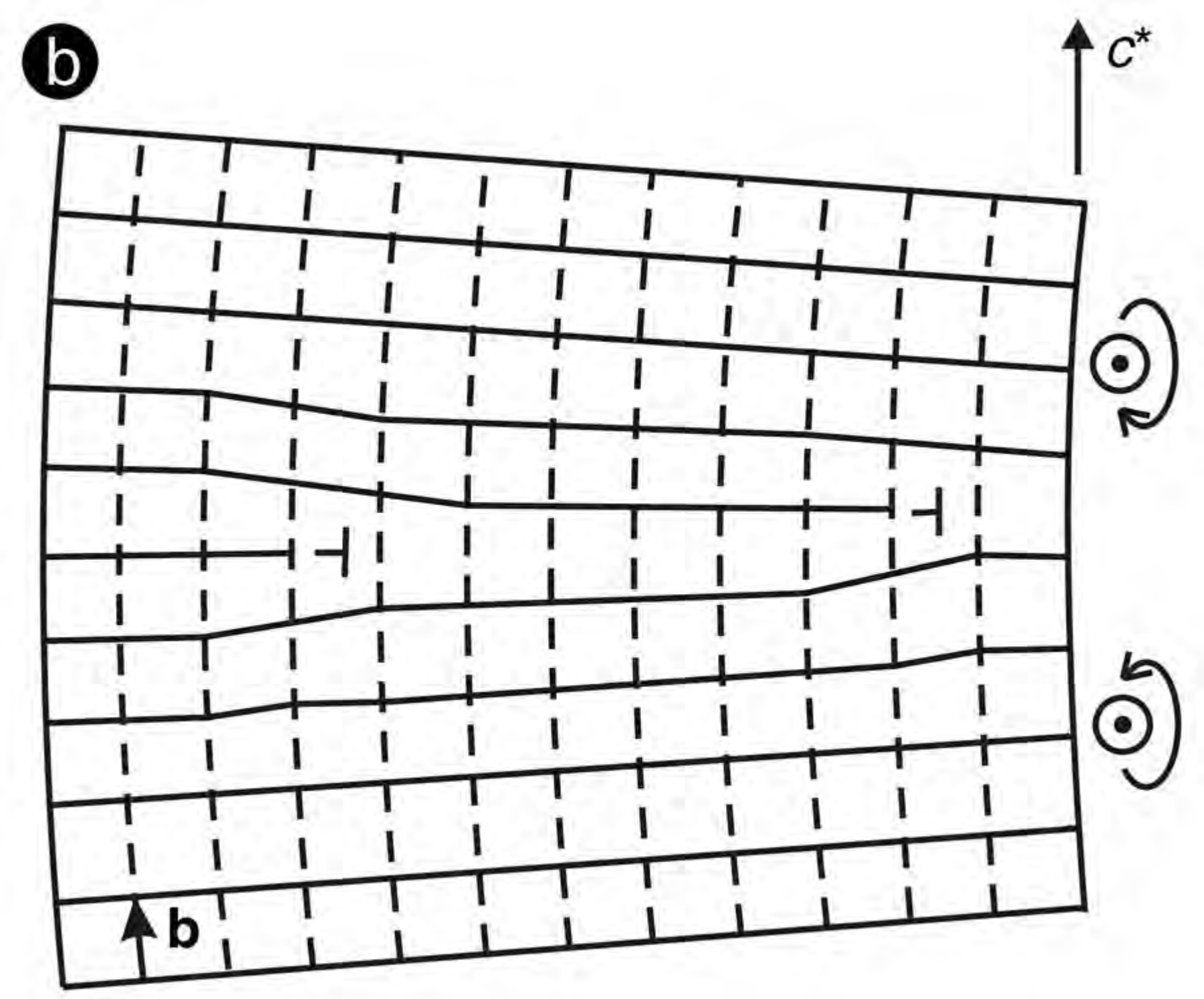

Figure 4b

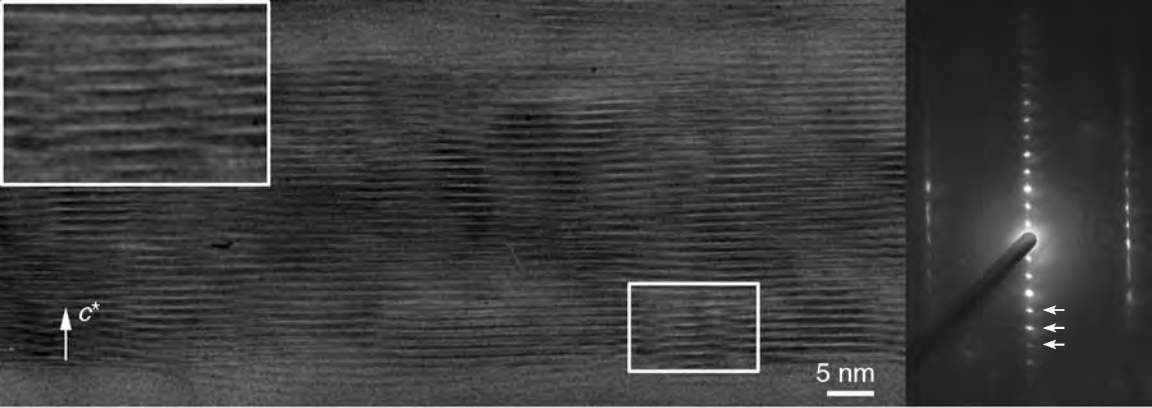

Figure 5

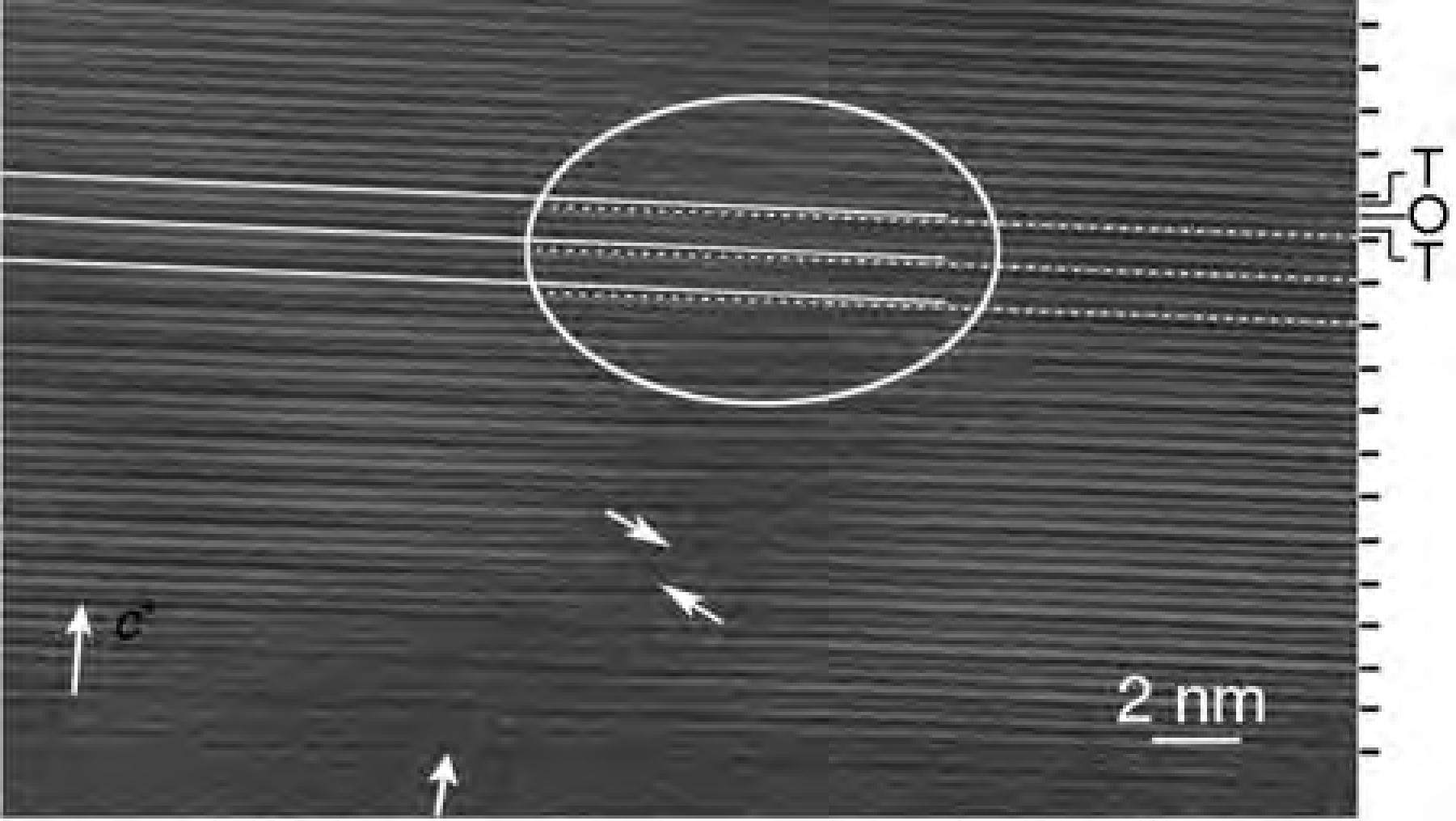

Figure 6

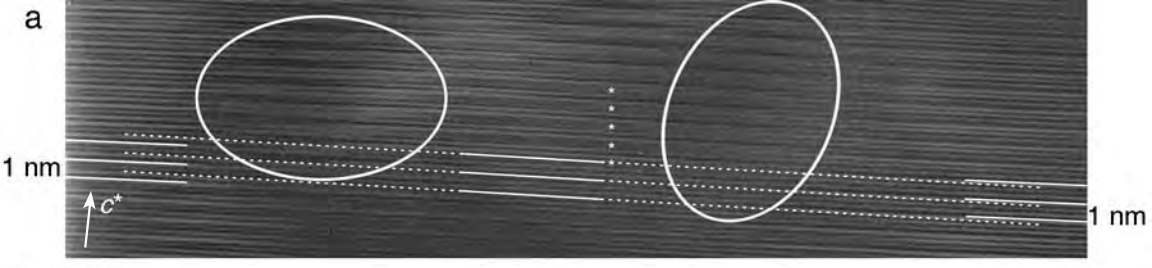

Figure 7a

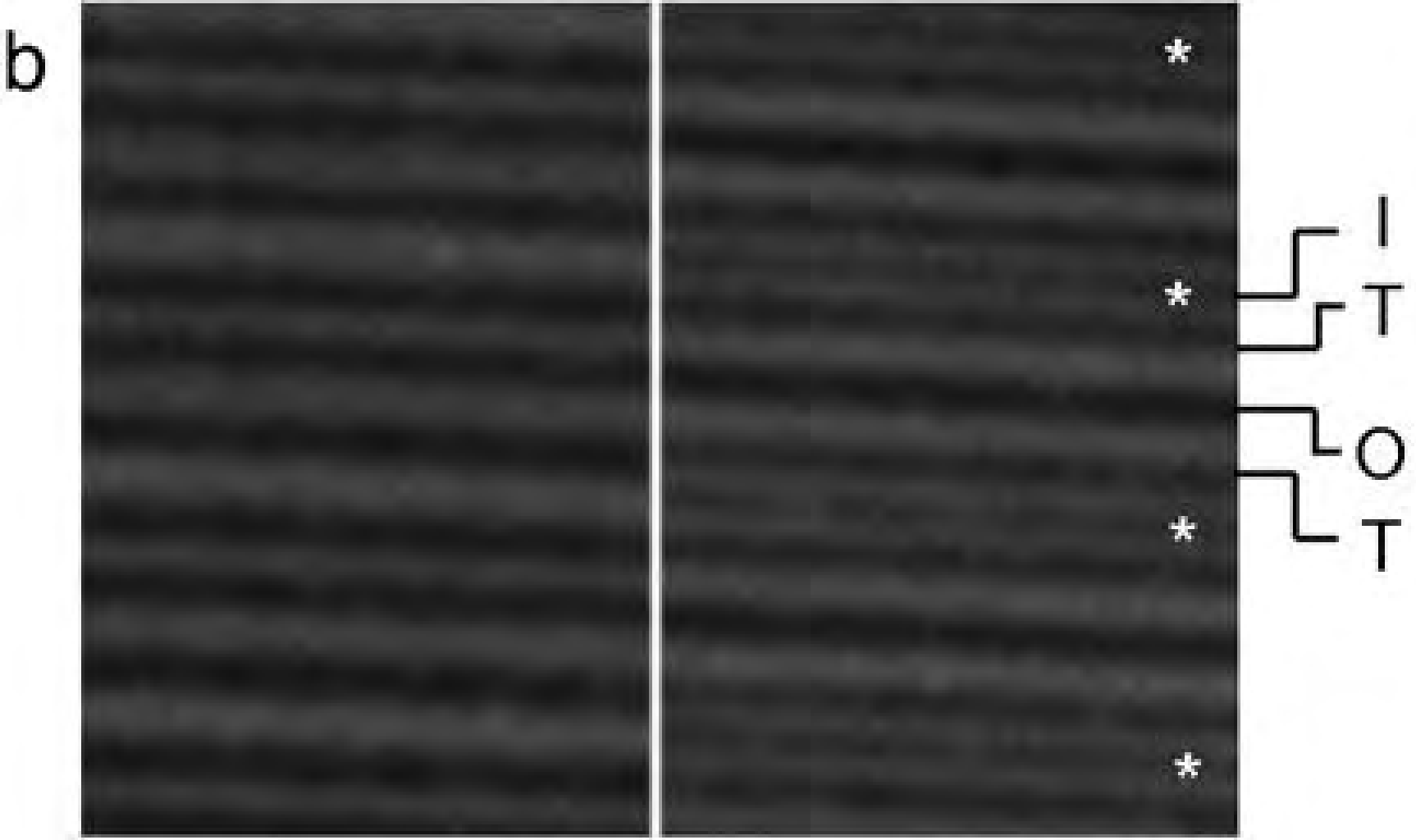

Figure 7b

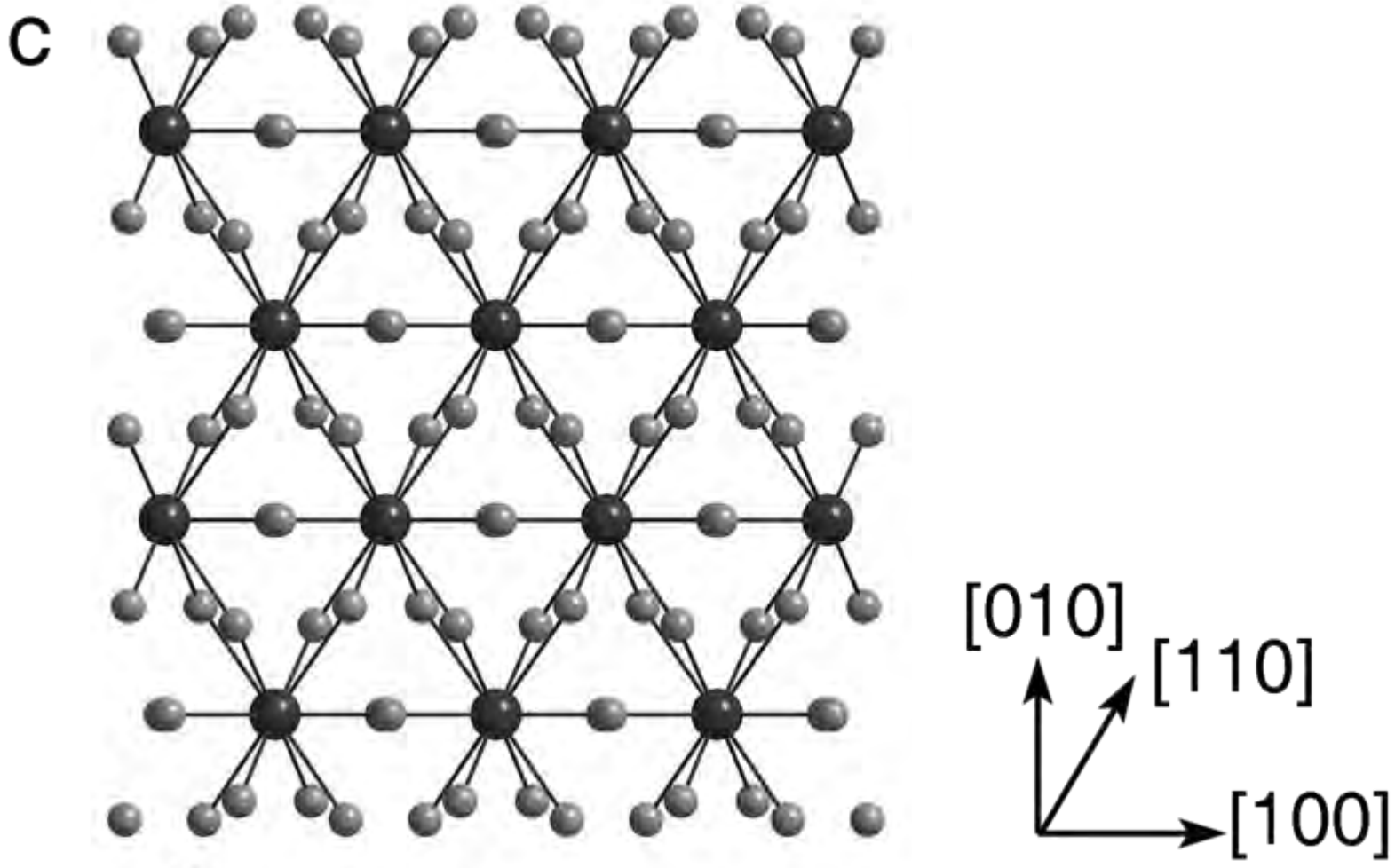

Figure 7c

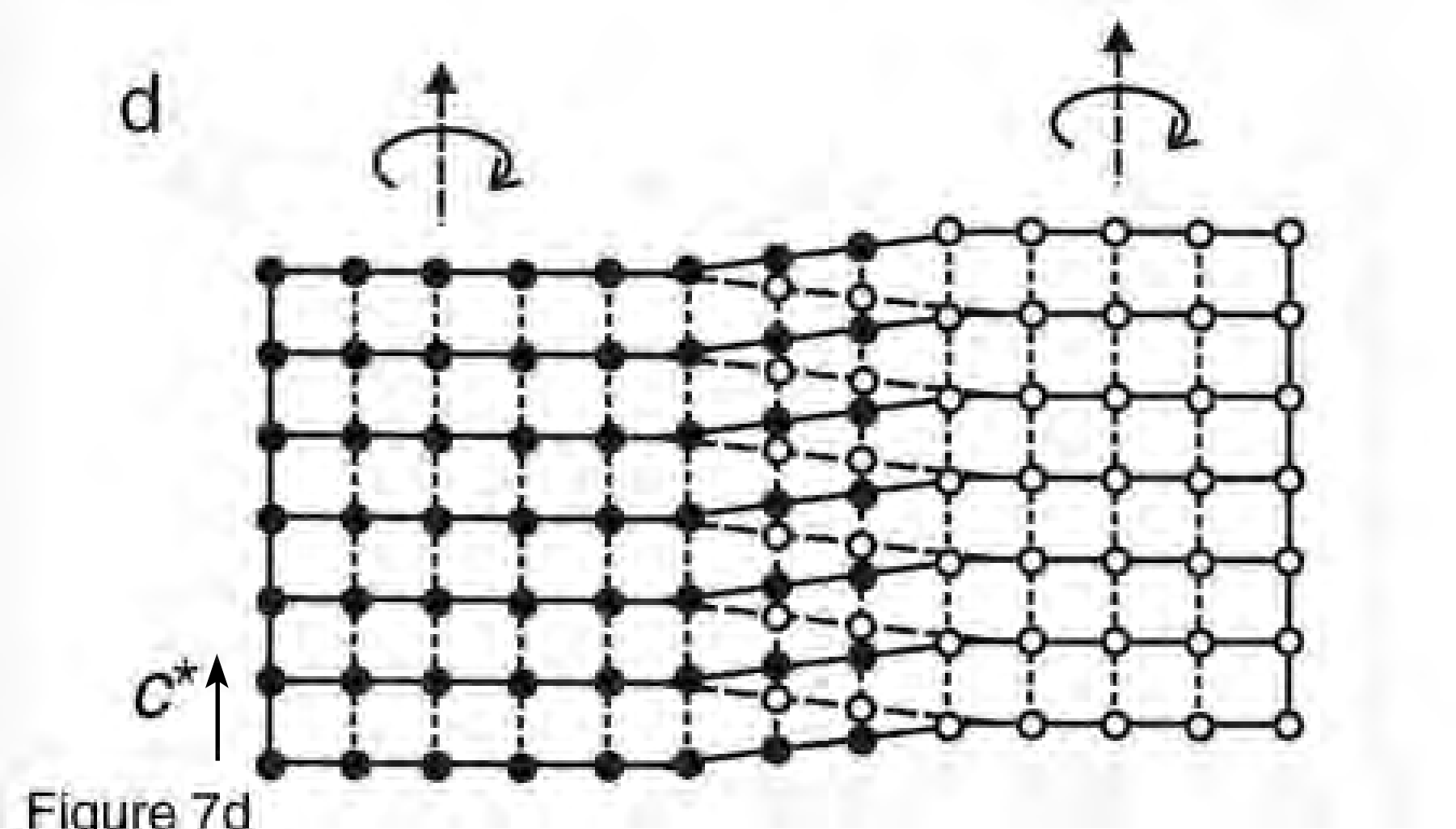

Figure 7d